Local stability of laser-welded stainless steel slender I-sections under combined loading

Hongdong Ran [a,b], Zhanpeng Chen [a], Yunmei Ma [c], Luigi Di Sarno [d], Yao Sun [e,f,*]

[a] School of Civil Engineering, Xi'an University of Architecture and Technology, Xi'an, China.
[b] Key Lab of Structural Engineering and Earthquake Resistance, Ministry of Education, Xi'an, China.
[c] China Northwest Architecture Design and Research Institute Co., Ltd, Xi'an, China.
[d] Department of Civil Engineering and Industrial Design, University of Liverpool, Liverpool, UK.
[e] School of Civil Engineering, University College Dublin, Dublin, Ireland.
[f] Department of Civil Engineering, Xi'an Jiaotong-Liverpool University, Suzhou, China.

* Corresponding author, Email: yao.sun@ucd.ie

Abstract

This paper presents a comprehensive experimental and numerical investigation into the local buckling behaviour of laser-welded stainless steel slender I-sections under combined compression and bending moment. A testing programme was firstly carried out, including initial local geometric imperfection measurements and eccentric compression tests on ten laser-welded stainless steel slender I-section stub column specimens. Following the testing programme, a numerical modelling programme was conducted. Finite element models were developed and validated against the test results, and then adopted to perform parametric studies to generate additional numerical data. The obtained test and numerical data were used to evaluate the applicability of the interaction curves in the European and American codes and the continuous strength method to laser-welded stainless steel slender I-sections under combined loading. The evaluation results generally show that the three sets of considered interaction curves offer adequate design accuracy for laser-welded stainless steel slender I-sections under combined compression and major-axis bending moment, but they yield unduly conservative and scattered resistance predictions for laser-welded stainless steel slender I-sections under minor-axis combined loading, owing principally to the conservative minor-axis bending end points. Finally, an improved design interaction curve for the minor-axis combined loading case was developed and shown to yield substantially more accurate and consistent resistance predictions for laser-welded stainless steel slender I-sections under minor-axis combined loading than the three considered design methods. The reliability of the new design interaction curve was confirmed based on a reliability study.

Keywords: Cross-sectional behaviour; Design codes; Eccentric compression tests; Laser-welding; New proposal; Stainless steel slender I-sections.

1. Introduction

Stainless steel has been increasingly used in building and structural engineering in recent years, owing to its favourable mechanical properties coupled with superior corrosion resistance and durability [1–5], which can greatly reduce the maintenance and inspection work. As an advanced fabrication technique, laser welding can minimise the input heat, which leads to reduced heat affected zones as well as low residual stresses and thermal distortions [6,7]. As a result, laser welding, which is also highly precise, is increasingly adopted for joining stainless steels to form various welded built-up section profiles. Comprehensive research into laser-welded stainless steel structural members with different cross-section profiles subjected to various loading conditions has been conducted, in order to verify their structural responses, examine the codified design rules, and develop improved design methods with good design accuracy and consistency. Previous experimental studies are firstly reviewed herein. Gardner et al. [6] and Ran et al. [8] conducted stub column tests on laser-welded stainless steel I-sections to investigate their cross-section compression resistances and local stability. Bu and Gardner [7] and Theofanous et al. [9] carried out in-plane bending tests on laser-welded stainless steel I-, channel and angle section beams, in order to examine their cross-section bending resistances. Liang et al. [10,11] experimentally investigated the cross-sectional behaviour of laser-welded stainless steel channel sections under combined compression and bending. The global stability of laser-welded stainless steel I- and angle section columns were studied by Gardner et al. [6], Ran et al. [8] and Filipović et al. [12] through a series of concentric compression tests. Bu and Gardner [13] and Kucukler et al. [14] investigated the structural performance of laterally unrestrained laser-welded stainless steel I-section beam-columns under minor-axis and major-axis combined loading, respectively. The literature review revealed that although in-depth research into the structural behaviour and resistances of laser-welded stainless steel components under various loading conditions has been previously conducted, cross-section responses and resistances of laser-welded stainless steel slender I-sections under combined loading remain unexplored, and therefore the present study was initiated.

In this paper, an experimental programme was firstly carried out, including eccentric compression tests on ten laser-welded stainless steel slender I-section stub columns and supplementary initial local geometric imperfection measurements. The obtained test results were used in a numerical modelling programme for establishing and validating finite element models; upon validation, the numerical models were adopted to perform parametric studies to generate additional numerical data. Based on the obtained test and numerical data, the applicability of the design interaction curves given in EN 1993-1-4 [15], ANSI/AISC 370-21 [16] and the continuous strength method [17] to laser-welded stainless steel slender I-sections under combined loading was evaluated. Finally, an improved interaction curve was proposed.

2. Experimental Study

2.1. General

Given that there have been no experimental results on laser-welded stainless steel I-sections under combined loading, a testing programme was firstly conducted to generate a test data pool. Two different I-sections – I-90×90×3 and I-120×90×3 were adopted in the testing programme, with five stub column specimens prepared for each I-section size. All the ten stub column specimens were fabricated through laser welding from 3 mm thick grade EN 1.4301 austenitic stainless steel hot-rolled plates, with the welding techniques and procedures following those given in EN ISO 13919-1 [18]. The two adopted I-sections are classified as Class 4 slender sections based on the slenderness limits set out in EN 1993-1-4 [15] and slender sections according to the cross-section classification framework given in ANSI/AISC

370-21 [16]. Overall, the testing programme comprised material testing and residual stress measurements, initial local geometric imperfection measurements and ten eccentric compression tests.

2.2. Material testing and membrane residual stress measurements

The material stress–strain responses and membrane residual stresses of the studied laser-welded stainless steel I-sections were carefully measured and fully reported by the authors in Ran et al. [8], with the experimental procedures and results briefly summarised herein. Two longitudinal coupons, extracted from the virgin plates with the geometric sizes in compliance with those given in EN ISO 6892-1 [19], were tested in a 300 kN testing machine subjected to displacement control. Fig. 1 shows the material stress–strain curves obtained from the tensile coupon tests, while Table 1 reports the key average measured material properties, including the Young's modulus E, the 0.2% proof stress f_y, 1.0% proof stress $f_{1.0}$, the ultimate stress f_u, the strain at the ultimate stress ε_u, the strain at fracture ε_f over a standard gauge length [20] and the coefficients used in the Ramberg–Osgood material model n and $m_{1.0}$ [21–24]. The membrane residual stresses in the studied laser-welded stainless steel I-sections were measured by means of the sectioning method, which has been broadly used in previous relevant membrane residual stress measurements [6,25–28], with the detailed procedures and results presented in Ran et al. [8]. The measured membrane residual stresses were found to be well captured by the residual stress predictive model proposed by Gardner et al. [6] for laser-welded stainless steel I-sections, with the pattern shown in Fig. 2 and the distribution parameters (a, b, c and d) presented in Table 2.

2.3. Initial local geometric imperfection measurements

As an important characteristic of thin-walled steel components, geometric imperfections may affect their structural performance. Initial local geometric imperfection measurements were thus conducted on the ten laser-welded stainless steel I-section stub column specimens. Fig. 3 shows the measurement setup, where a stub column specimen is fixed on the moving bench of a milling machine through the use of a vise and a percentage gauge with 0.01 mm precision is tightly mounted onto the machine head to measure the local deviations of each constituent plate element. This measurement setup has been successfully used in previous relevant studies [6–8,10,11,26–29] and was thus also employed in this study. The local imperfection measurements were performed on the cross-sections at mid-height and two third points of the specimen length. For each constituent plate element of the stub column specimen, the initial local geometric imperfections were defined as the deviations from a linear reference line fitted to the corresponding measured data set, while the maximum deviation obtained from the three cross-sections was taken as the initial local geometric imperfection magnitude ω_0 of the stub column specimen, as presented in Table 3. The normalised value ω_0/b_f for each stub column specimen is also given in Table 3, where b_f is the flange width, showing that the largest normalised value ω_0/b_f from all the stub column specimens is 1/257, less than the fabrication tolerance value of 1/100 recommended in EN 1993-1-5 [30].

2.4. Eccentric compression tests

Eccentric compression tests were carried out on the ten laser-welded stainless steel slender I-section stub column specimens, with six conducted about the major principal axis and four performed about the minor principal axis, in order to investigate their structural performance under combined compression and bending. The geometric dimensions of the ten stub column specimens were measured, as presented in Table 3, including the specimen length L, the outer section height h, the flange width b_f and the plate thickness t. For each stub column specimen, its end sections were then welded with a pair of 6 mm thick flat steel plates. All the eccentric compression tests were conducted in an INSTRON testing machine. The adopted initial loading eccentricities were varied between 5 mm and 80 mm and therefore a wide range of loading combinations were considered in the tests. Pin-ended boundary conditions were applied to each stub column specimen; this was achieved through the use of a pair of knife-edge devices, which were respectively mounted onto the top and bottom ends of the testing machine. As shown in Fig. 4, each knife-edge device comprises a wedge plate with a knife edge and a pit plate with a semi-circular groove. Before testing, each stub column specimen was firstly placed between the top and bottom knife-edge devices, with their relative position adjusted to achieve pre-specified loading eccentricity and proper member alignment. Then, each specimen was fixed to the knife-edge devices through bolting.

Fig. 4 shows the apparatus used for the eccentric compression tests, including six LVDTs and four strain gauges. The strain gauges were attached to the external surfaces of the two flanges at the specimen mid-height to measure the longitudinal strains at these positions. LVDT-1 to LVDT-4 were used to measure the rotations at the top and bottom ends, LVDT-5 was adopted to monitor the end shortening of each specimen, and LVDT-6 was placed at the specimen mid-height to measure the corresponding lateral deflection. Once the test setup was completed, a loading rate of 0.2 mm/min was adopted to drive the testing machine to eccentrically compress each stub column specimen. The longitudinal strains obtained from the two pairs of strain gauges, together with the mid-height lateral deflections measured from LVDT-6, were used to determine the actual initial loading eccentricity e_0 of each stub column specimen, based on Eq. (1) [31–33], where I is the second moment of area about the axis of combined loading, ε_{max}–ε_{min} is the longitudinal strain difference, N is the applied compression load and D is the distance between the two pairs of strain gauges, respectively equal to h and b_f–$2d_s$ for the major-axis and minor-axis combined loading cases, as graphically depicted in Fig. 5. Note that Eq. (1) was derived based on the assumption that the structural behaviour was close to linear elastic, it was suggested that the eccentric compression loads employed for calculating e_0 be lower than 15% of the estimated failure loads.

$$e_0 = \frac{EI\left(\varepsilon_{\max} - \varepsilon_{\min}\right)}{ND} - \Delta \tag{1}$$

The failure modes of the tested laser-welded stainless steel I-section stub column specimens under minor-axis and major-axis combined loading are displayed in Fig. 6(a) and Fig. 6(b), respectively, showing significant local buckling coupled with overall flexural deformation about the axis of combined loading. Fig. 7 presents the full load–end rotation curves for the two series of tested specimens, while Table 4 presents the key test results, including the actual initial loading eccentricity e_0, the failure load N_u, the end rotation at the failure load ϕ_u and the corresponding load shortening δ_u and mid-height lateral deflection Δ_u, and the failure moment at the specimen mid-height $M_u=N_u(e_0+\Delta_u)$, Within each specimen series, the stub columns with larger initial loading eccentricities have lower ultimate loads but larger lateral deflections at mid-height, due to the increased effect from bending.

3. Numerical Modelling

3.1. General

In this section, a numerical modelling programme was carried out by means of the nonlinear finite element (FE) analysis package ABAQUS [34] to supplement the testing programme. FE models on laser-welded stainless steel slender I-section stub column specimens under combined loading were developed and validated against the obtained test results. Upon validation, the developed FE models were employed to perform parametric studies to generate additional numerical data over a wide range of cross-section dimensions and loading combinations.

3.2. Development and validation of FE models

The 'S4R' shell element [34] has been proven to be able to well simulate various stainless steel welded I-section members [7,8,13,14,26,32,33,35–37] and was thus adopted herein.

Based on a prior study on the mesh sensitivity, the element length and width were selected as 1.5*t* and *t*, respectively, which were found to (i) lead to an accurate incorporation of the membrane residual stresses into the FE models and (ii) result in good computational efficiency and accuracy. Regarding the material modelling of the used austenitic stainless steel, the engineering stress–strain response, measured from the material test on Coupon #1 (see Fig. 1), was converted into the true stress–strain response and then inputted into ABAQUS [34]. The membrane residual stresses in each laser-welded stainless steel I-section stub column were firstly derived from the predictive model, as depicted in Fig. 2 and Table 2, and then incorporated into the corresponding FE model using the '*INITIAL CONDITIONS' command [34]. Fig. 8 shows the membrane residual stresses incorporated into the numerically modelled I-90×90×3 specimens. Upon successful incorporation of the material response and membrane residual stresses, the experimentally adopted pin-ended boundary and eccentric loading conditions were carefully modelled in the development of the FE models. Specifically, for each FE model, its top and bottom end sections were respectively coupled to one reference point that was located (i) longitudinally at a distance of 80 mm away from the corresponding end section and (ii) eccentrically to the combined loading axis with the eccentricity given as the corresponding actual eccentricity e_0. The top reference point can rotate about the combined loading axis and translate longitudinally, while the bottom reference point only has the rotation about the same axis. The initial local geometric imperfections were also included into each FE model, with the distribution pattern taken as the lowest elastic local buckling mode shape, as derived from a prior elastic eigenvalue buckling analysis [34]. Two local imperfection magnitudes, including the measured value ω_0 and a generalised value $b_f/300$, were adopted to factor the obtained local imperfection distribution profiles.

Once the FE models were developed, each of them was analysed through the materially and geometrically nonlinear 'Static, Riks' analysis [34], in order to derive the numerical results, including the numerical failure load, load–end rotation curve and failure mode. The accuracy of the developed FE models was evaluated through quantitative and graphical comparisons between the derived numerical results and their experimental counterparts. The quantitative comparison results were presented in Table 5, where the FE-to-test failure loads for the stub column specimens are reported, showing that all the two adopted local imperfection magnitudes led to accurate predictions of experimental failure loads; this reflected the insensitivity of the developed FE models to initial local geometric imperfection magnitudes. Graphical comparisons between the test and FE load–end rotation curves for the two series of stub column specimens are presented in Fig. 7, where the experimental responses are accurately captured by their FE counterparts. Moreover, the experimentally obtained failure modes were found to be well simulated by the developed FE models, as shown in Fig. 9(a) and Fig. 9(b) for two typical specimens 90-MI2 and 90-MA3. Upon the quantitative and graphical comparisons, the developed FE models have been shown to be capable of simulating the structural performance of laser-welded stainless steel slender I-sections under combined loading and were thus considered to be validated.

3.3. Parametric studies

Upon validation, the developed FE models were adopted to carry out parametric studies to expand the test data pool over a wide range of cross-section dimensions and loading combinations, beyond those considered in the testing programme. Regarding the modelled I-sections, their cross-section dimensions were carefully selected, ensuring that they were classified as slender I-sections by both EN 1993-1-4 [15] and ANSI/AISC 370-21 [16]. Table 6 reports the cross-section dimensions and loading eccentricities used in the parametric studies. Specifically, both the outer section height h and flange width b_f were varied from 60 mm to 150 mm, with the plate thickness t varied between 2 mm and 3 mm, leading to a broad spectrum of cross-section dimensions and aspect ratios being examined. The cross-sectional slendernesses [17] were varied from 0.72 to 1.65. It is worth noting that the maximum cross-sectional slenderness of the specimens is 0.80; therefore, the numerical results for I-sections with slenderness greater than 0.80 may require a validation in the future based on further eccentric compression tests. The model length was equal to $3h$ [25]. Moreover, the initial loading eccentricities were varied between 1 mm and 100 mm, leading to a wide spectrum of loading combinations being considered. All the FE models were developed through employing the modelling assumptions, techniques and procedures detailed in Section 3.2, but their local imperfection magnitudes were kept at $b_f/300$. The engineering stress–strain response measured from the material test on Coupon #1 (see Fig. 1) was converted into the true stress–strain response and then used in the parametric studies. In total, 400 numerical data on laser-welded stainless steel slender I-sections under combined loading were derived through the parametric studies, with 200 for each principal axis.

4. Design Analysis

4.1. General

In this section, the applicability of the design interaction curves given in EN 1993-1-4 [15], AISC/AISC 370-21 [16] and the continuous strength method [17] to laser-welded stainless steel slender I-sections under combined compression and bending was evaluated by comparing the test and FE failure loads N_u against the unfactored design failure loads $N_{u,pred}$. A new design method was also proposed for laser-welded stainless steel slender I-sections under minor-axis combined loading, underpinned by the test and FE data. Table 7 presents the quantitative evaluation of the considered and proposed design methods, where the mean test and numerical to predicted failure load ratios $N_u/N_{u,pred}$ and the corresponding coefficients of variance (COVs) are reported, while Figs 10–13 show the graphical evaluation results, where the test and numerical data are plotted against the considered and proposed design interaction curves, respectively.

4.2. EN 1993-1-4 (EC3)

The current Eurocode EN 1993-1-4 [15] adopts similar design rules for stainless steel structures as those given in EN 1993-1-1 [38] for mild steel structures. Regarding Class 4 slender I-sections under combined loading, the Eurocodes [15,38] use a linear interaction curve, as given by Eq. (2), where $N_{\mathrm{u,pred}}$ is the design failure load and $M_{\mathrm{u,y}}$ (or $M_{\mathrm{u,z}}$)=$N_{\mathrm{u,pred}}(e_0+\Delta_{\mathrm{u}})$ is the design major-axis (or minor-axis) failure moment, while $N_{\mathrm{eff,EC3}}=A_{\mathrm{eff,EC3}}f_{\mathrm{y}}$ is the EC3 effective cross-section compression capacity, and $M_{\mathrm{eff,y}}=W_{\mathrm{eff,y}}f_{\mathrm{y}}$ and $M_{\mathrm{eff,z}}=W_{\mathrm{eff,z}}f_{\mathrm{y}}$ are the EC3 effective cross-section bending capacities about the major axis and minor axis, respectively, where $A_{\mathrm{eff,EC3}}$ is the EC3 effective cross-section area, and $W_{\mathrm{eff,y}}$ and $W_{\mathrm{eff,z}}$ are the EC3 effective section moduli about the major axis and minor axis, respectively.

$$\frac{N_{\mathrm{u,pred}}}{N_{\mathrm{eff,EC3}}}+\frac{M_{\mathrm{u,y}}}{M_{\mathrm{eff,y}}}+\frac{M_{\mathrm{u,z}}}{M_{\mathrm{eff,z}}}=1 \tag{2}$$

The values of $A_{\mathrm{eff,EC3}}$, $W_{\mathrm{eff,y}}$ and $W_{\mathrm{eff,z}}$ can be determined through using the EC3 effective width approach. Specifically, $A_{\mathrm{eff,EC3}}$ is calculated as the summation of the effective area of each constituent plate element that is taken as its effective width c_{eff} multiplied by its thickness t. The effective width c_{eff} can be calculated from Eq. (3), where c is the flat plate width and $\bar{\lambda}_{\mathrm{l}}$ is the plate slenderness, as given by Eq. (4), in which k_σ is the buckling parameter and given as 4.0 and 0.43 for internal and outstand plate elements [30], respectively. With regard to the calculation of $W_{\mathrm{eff,y}}$ and $W_{\mathrm{eff,z}}$, Eqs (3) and (4) are still used, but the value of k_σ is different now and dependent on the plate element type (i.e. outstand or internal) and the stress distribution subjected to bending, as derived based on Table 4.1 and Table 4.2 of EN 1993-1-5 [30].

$$c_{\mathrm{eff}} = \begin{cases} c\left(\dfrac{1}{\overline{\lambda}_1} - \dfrac{0.188}{\overline{\lambda}_1^{\,2}}\right) \le c & \text{for outstand elements} \\ c\left(\dfrac{0.772}{\overline{\lambda}_1} - \dfrac{0.079}{\overline{\lambda}_1^{\,2}}\right) \le c & \text{for internal elements} \end{cases} \tag{3}$$

$$\overline{\lambda}_1 = \frac{c/t}{28.4\sqrt{235E/\left(210000 f_{\mathrm{y}}\right)}\sqrt{k_{\sigma}}} \tag{4}$$

Based on the obtained test and FE data, the applicability of the EC3 design interaction curve to laser-welded stainless steel slender I-sections under combined loading was evaluated. Graphical evaluation was firstly carried out, with the evaluation results shown in Fig. 10(a) and Fig. 10(b) for minor-axis and major-axis combined loading cases, where the test and numerical failure moments and loads, plotted in a normalised format ($M_{\mathrm{u}}/M_{\mathrm{eff}}$ versus $N_{\mathrm{u}}/N_{\mathrm{eff,EC3}}$), are compared against the EC3 linear interaction curve. It was evident that (i) the EC3 design interaction curve for minor-axis combined loading lies well below the normalised test and FE data points, indicating excessive conservatism and scatter, and (ii) its major-axis combined loading counterpart can well represent the corresponding data points. This can be also proven from the quantitative evaluation results presented in Table 7(a), with the mean test and numerical to predicted failure load ratios $N_{\mathrm{u}}/N_{\mathrm{u,pred}}$ for minor-axis and major-axis combined loading cases equal to 1.64 and 1.15, and the corresponding COVs of 0.11 and 0.09. Given that the EC3 effective compression capacity $N_{\mathrm{eff,EC3}}$ (i.e. the compression end point) is accurate [8,26], the conservatism and scatter of the EC3 design interaction curve for the minor-axis combined loading case are due principally to the use of the conservative minor-axis bending end point (i.e. the effective moment capacity $M_{\mathrm{eff,z}}$) [7,26].

4.3. ANSI/AISC 370-21 (AISC)

The design rules given in the American specification ANSI/AISC 370-21 [16] for stainless steel doubly symmetric cross-sections under combined loading are the same as those set out in the mild steel design specification ANSI/AISC 360-16 [39]. Specifically, the American specifications [16,39] adopt a bi-linear interaction curve to predict the cross-section resistances of slender I-sections under combined compression and bending, as given by Eq. (5), where $N_{\mathrm{eff,AISC}}=A_{\mathrm{eff,AISC}}f_{\mathrm{y}}$ is the AISC effective cross-section compression capacity and M_{cy} and M_{cz} are respectively the AISC cross-section effective major-axis and minor-axis bending capacities, as determined according to Chapter F.5 and F.6 specified in ANSI/AISC 370-21 [16].

$$\begin{cases} \dfrac{N_{\mathrm{u,pred}}}{N_{\mathrm{eff,AISC}}}+\dfrac{8}{9}\left(\dfrac{M_{\mathrm{u,y}}}{M_{\mathrm{cy}}}+\dfrac{M_{\mathrm{u,z}}}{M_{\mathrm{cz}}}\right)=1.0 \quad \text{for} \quad \dfrac{N_{\mathrm{u,pred}}}{N_{\mathrm{eff,AISC}}}\geq 0.2 \\ \dfrac{N_{\mathrm{u,pred}}}{2N_{\mathrm{eff,AISC}}}+\left(\dfrac{M_{\mathrm{u,y}}}{M_{\mathrm{cy}}}+\dfrac{M_{\mathrm{u,z}}}{M_{\mathrm{cz}}}\right)=1.0 \quad \text{for} \quad \dfrac{N_{\mathrm{u,pred}}}{N_{\mathrm{eff,AISC}}}< 0.2 \end{cases} \tag{5}$$

The cross-section resistance predictions for laser-welded stainless steel slender I-sections under combined loading, as determined from the AISC bi-linear interaction curve, were quantitatively evaluated against the test and numerical results. Table 7(b) presents the quantitative evaluation results, where the mean test and numerical to AISC design failure load ratios $N_{\mathrm{u}}/N_{\mathrm{u,pred}}$ for minor-axis and major-axis combined loading cases are equal to 1.61 and 1.11, respectively. In parallel with the quantitative evaluation, a graphical evaluation was also performed and shown in Fig. 11, where the experimentally and numerically obtained failure bending moments and axial loads are normalised by the cross-section effective moment capacities and cross-section effective compression capacities, and compared with the AISC bi-linear interaction curve. Both the quantitative and graphical evaluations revealed that (i) the AISC design interaction curve yields overall good design accuracy when applied to laser-welded stainless steel slender I-sections under major-axis combined loading, but with many over-predicted failure load predictions, and (ii) the AISC design interaction curve results in overly conservative and scattered failure load predictions when used for laser-welded stainless steel slender I-sections under minor-axis combined loading, owing mainly to the conservative minor-axis bending end point (M_{cz}).

4.4. Continuous strength method (CSM)

The continuous strength method (CSM) [17,40] is a recently developed strain-based design method for stainless steel components. For stainless steel slender sections under combined loading, the CSM also adopts the linear interaction curve but with the CSM cross-section bending ($M_{csm,y}$ and $M_{csm,z}$) and compression (N_{csm}) capacities, as given by Eq. (6).

$$\frac{N_{u,pred}}{N_{csm}}+\frac{M_{u,y}}{M_{csm,y}}+\frac{M_{u,z}}{M_{csm,z}}=1 \tag{6}$$

To calculate the CSM cross-section capacities, the first step lies in determination of the cross-section (compressive) limiting strain ε_{csm} that reflects the deformation capacity of the examined slender I-section under the applied loading. This can be achieved by using the 'base curve' [17], as given by Eq. (7), where $\varepsilon_y = f_y/E$ is the yield strain, $\bar{\lambda}_p = \sqrt{f_y/f_{cr}}$ is the cross-section slenderness, in which f_{cr} is the critical elastic buckling stress of the examined I-section under the applied loading and can be determined by means of the finite-strip package CUFSM [41]. Once the limiting strain ε_{csm} is determined, the CSM design compressive stress σ_{csm} can be calculated as ε_{csm} multiplied by the material Young's modulus E, as given by Eq. (8). Then, the CSM cross-section compression capacity (N_{csm}) and bending capacities ($M_{csm,y}$ and $M_{csm,z}$) are determined by using Eq. (9) and Eq. (10), respectively.

$$\frac{\varepsilon_{csm}}{\varepsilon_y} = \left(1 - \frac{0.222}{\bar{\lambda}_p^{1.05}}\right)\frac{1}{\bar{\lambda}_p^{1.05}} \tag{7}$$

$$f_{csm} = E\varepsilon_{csm} \tag{8}$$

$$N_{csm} = Af_{csm} \tag{9}$$

$$\begin{cases} M_{csm,y} = W_{el,y} f_{csm} \\ M_{csm,z} = W_{el,z} f_{csm} \end{cases} \tag{10}$$

The test and numerical failure moments and loads were normalised by the corresponding M_{csm} and N_{csm}, and are plotted together with the CSM interaction curves in Fig. 12(a) and Fig. 12(b) for minor-axis and major-axis combined loading cases, respectively, where the CSM interaction curve for major-axis combined loading is shown to be capable of well representing the normalised test and FE data while its minor-axis combined loading counterpart lies far below the test and FE data. The graphical evaluation was followed by a quantitative evaluation, with the results given in Table 7(c), where the mean load ratios $N_u/N_{u,pred}$ for minor-axis and major-axis combined loading cases are equal to 1.58 and 1.12. The quantitative and graphical evaluations indicated that similar to the EC3 design interaction curve, the CSM interactive curve provides good design accuracy and consistency for laser-welded stainless steel slender I-sections under major-axis combined loading, but it leads to conservative cross-section resistances predictions for those under minor-axis combined loading, due mainly to the conservative CSM minor-axis bending end point [7,26]. Therefore, new interaction curves that are capable of yielding accurate failure load predications for laser-welded stainless steel slender I-sections under minor-axis combined loading are required.

4.5. New design method for minor-axis combined loading

The analyses and discussions in Section 4.2 have highlighted that the current EC3 interaction curve for laser-welded stainless steel slender I-sections under minor-axis combined loading has an accurate compression end point but a conservative minor-axis bending end point. An improved design method is therefore proposed by adopting the EC3 interaction curve anchored to a more accurate minor-axis bending end point. As highlighted in previous research [42,43] on the behaviour of steel slender I-sections under minor-axis bending, it is incorrect to assume the linear elastic stress distribution within the slender outstand flanges and plasticity can develop in both compressive and tensile parts. To address the conservatism, the plastic effective width method [42] was developed to consider the plastic reserve capacities of slender steel I-sections in minor-axis bending, and has been proven to yield accurate bending capacity predictions when applied to stainless steel slender I-sections in minor-axis bending [43]. Therefore, the plastic effective width method is ideal to be used to determine the new minor-axis bending end points. The new interaction curve is given by Eq. (11), where $M_{p,eff,z}$ is the effective minor-axis bending capacity determined by the plastic effective width method.

$$\frac{N_{u,pred}}{N_{eff,EC3}}+\frac{M_{u,z}}{M_{p,eff,z}}=1 \tag{11}$$

In calculation of $M_{p,eff,z}$, the plastic effective width method determines the effective cross-section based on the strain and stress distributions depicted in Fig. 14 [42,43]. It is assumed that (i) the maximum attainable compressive strain is equal to the yield strain multiplied by a coefficient C_y=3 and (ii) the plastic compressive region is at a distance of e_{cc}=0.225b_f from the web centreline, with the region width of b_e determined from Eq. (12). The location of the neutral axis can then be determined according to the stress equilibrium, as given by Eq. (13), and the effective minor-axis bending capacity $M_{p,eff,z}$ can be calculated through integrating the stress distribution, as given by Eqs (14)–(19). Note that the definitions of the notations in Eqs (13)–(19) are graphically illustrated in Fig. 14.

$$b_e=0.2b_f\overline{\lambda}_p^{-0.75} \tag{12}$$

$$x_p=\frac{2b_et_f[(b_f-b_e/2)-(0.5b_f-b_e-e_{cc})]+b_ft_fb_f/4+(h-2t_f)t_wb_f/2}{2b_et_f+b_ft_f+(h-2t_f)t_w} \tag{13}$$

$$M_{p,eff,z}=2b_et_ff_y\left(e_{cc}+\frac{b_e}{2}+c\right)+2b_pt_ff_y\left(x_p-\frac{b_p}{2}\right)+\frac{2}{3}b_g^2f_yt_f+\frac{2}{3}c^2f_wt_f+\left(h-2t_f\right)t_wf_wc \tag{14}$$

$$\text{where}\quad b_p=x_p-b_g \tag{15}$$

$$b_g=\varepsilon_y/K \tag{16}$$

$$K=\frac{C_y\varepsilon_y}{0.5b_f-x_p+e_{cc}+b_e} \tag{17}$$

$$c=0.5b_f-b_g-b_p \tag{18}$$

$$f_w = cKE \tag{19}$$

The normalised test and numerical failure moments ($M_u/M_{peff,z}$) and loads ($N_u/N_{eff,EC3}$) are plotted against the new design interaction curve in Fig. 13, where the new interaction curve displays a much better representation of the normalised data points in comparison with its EC3, AISC and CSM counterparts in Figs 10–12, revealing the substantially improved design accuracy and consistency. This is also evident in Table 7(d), where the mean load ratio $N_u/N_{u,pred}$ is equal to 1.21, with the corresponding COV of 0.07, indicating that the proposed new interaction curve leads to significantly more accurate and consistent failure load predictions for laser-welded stainless steel slender I-sections under minor-axis combined loading than the three considered methods [15–17].

The reliability of the new design interaction curve when applied to laser-welded stainless steel slender I-sections under minor-axis combined loading was assessed herein, according to the requirements and procedures given in EN 1990 [44]. In the present reliability analysis, the material over-strength ratio for austenitic stainless steel and the corresponding COV were taken as 1.3 and 0.06, respectively, and the COV of the geometric properties of stainless steel cross-sections was taken as 0.05, following the recommendations of Afshan et al. [45]. The key statistical parameters calculated according to EN 1990 [44] are presented in Table 8, where $k_{d,n}$ is the design (ultimate limit state) fractile factor, b is the mean ratio of the test and numerical to design model resistances, V_δ is the COV of the test and numerical resistances relative to the resistance model, V_r is the combined COV incorporating both model and basic variable uncertainties, and γ_{M1} is the partial safety factor. The resulting (required) partial safety factor for the EC3 design rules, as reported in Table 8, is equal to 0.99, less than the current used value of 1.1 in EN 1993-1-4 [15], therefore demonstrating the reliability of the new design method when applied to laser-welded stainless steel slender I-sections under minor-axis combined loading.

5. Conclusions

A thorough testing and numerical modelling programme has been performed to investigate the cross-section resistances and local stability of laser-welded stainless steel slender I-sections under combined compression and bending. A testing programme was firstly conducted, which included initial local geometric imperfection measurements and eccentric compression experiments on ten laser-welded stainless steel slender I-section stub column specimens, with the test procedures and results fully presented. The testing programme was supplemented by a numerical simulation programme, in which FE models were developed and validated against the test observations. Upon validation, the FE models were employed to perform parametric studies to generate a numerical data pool over a broad range of cross-section dimensions and loading combinations. Then, the obtained test and numerical data were used to graphically and quantitatively evaluate the applicability of the design interaction curves given in EN 1993-1-4 [15], ANSI/AISC 370-21 [16] and the CSM [17] for laser-welded stainless steel slender I-sections under combined loading. The evaluation results generally indicated that all the considered EC3, AISC and CSM interaction curves offer good design accuracy for laser-welded stainless steel slender I-sections under major-axis combined loading, but lead to overly conservative and scattered cross-section resistance predictions for their counterparts under minor-axis combined loading, owing principally to unduly conservative minor-axis bending end points. To address this shortcoming, an improved design interaction curve was proposed for laser-welded stainless steel slender I-sections under minor-axis combined loading, which adopts the EC3 interaction curve anchored to a more accurate minor-axis bending end point. The proposed interaction curve was shown to offer substantially improved design accuracy and consistency than the three considered curves. A reliability analysis was then performed to confirm the reliability of the proposed design interaction curve.

Acknowledgements

The corresponding author would like to thank the assistance from his research fellow Dr Yinying Tao in the numerical modelling programme. The financial support from XJTLU Research Development Fund (No. RDF-21-01-008) is also acknowledged.

References

[1] L. Gardner, The use of stainless steel in structures, Prog. Struct. Eng. Mater. 7 (2) (2005) 45–55.

[2] L. Di Sarno, A.S. Elnashai, D.A. Nethercot. Seismic retrofitting of framed structures with stainless steel. J. Constr. Steel Res. 62(1-2) (2006) 93–104.

[3] N.R. Baddoo, Stainless steel in construction: A review of research, applications, challenges and opportunities, J. Constr. Steel Res. 64 (11) (2008) 1199–1206.

[4] L. Soufeiani, Foliente G., Nguyen K.T.Q., R. San Nicolas. Corrosion protection of steel elements in façade systems–A review. J. Build. Eng. 32 (2020) 101759.

[5] L. Di Sarno, A.S. Elnashai, D.A. Nethercot. Seismic response of stainless steel braced frames. J. Constr. Steel Res. 64 (7-8) (2008) 914–925.

[6] L. Gardner, Y. Bu, M. Theofanous, Laser-welded stainless steel I-sections: Residual stress measurements and column buckling tests, Eng. Struct. 127 (2016) 536–548.

[7] Y. Bu, L. Gardner, Local stability of laser-welded stainless steel I-sections in bending, J. Constr. Steel Res. 148 (2018) 49–64.

[8] H. Ran, Z. Chen, Y. Ma, Experimental and numerical studies of laser-welded slender stainless steel I-section columns, Thin-Walled Struct. 171 (2022) 108832.

[9] M. Theofanous, A. Liew, L. Gardner, Experimental study of stainless steel angles and channels in bending, Structures 4 (2015) 80–90.

[10] Y. Liang, O. Zhao, Y. Long, L. Gardner, Stainless steel channel sections under combined compression and minor axis bending – Part 1: Experimental study and numerical modelling, J. Constr. Steel Res. 152 (2019) 154–161.

[11] Y. Liang, O. Zhao, Y. Long, L. Gardner, Experimental and numerical studies of laser-welded stainless steel channel sections under combined compression and major axis bending moment, Thin-Walled Struct. 157 (2020) 107035.

[12] A. Filipović, J. Dobrić, D. Buđevac, N. Fric, N. Baddoo, Experimental study of laser-welded stainless steel angle columns, Thin-Walled Struct. 164 (2021) 107777.

[13] Y. Bu, L. Gardner, Laser-welded stainless steel I-sections beam-columns: Testing, simulation and design, Eng. Struct. 179 (2019) 23–36.

[14] M. Kucukler, L. Gardner, Y. Bu, Flexural-torsional buckling of austenitic stainless steel I-section beam-columns: Testing, numerical modelling and design, Thin-Walled Struct. 152 (2020) 106572.

[15] EN 1993-1-4:2006+A1:2015, Eurocode 3: Design of Steel Structures — Part 1-4: General Rules — Supplementary Rules for Stainless Steels, Including Amendment A1, European Committee for Standardization (CEN), Brussels, 2015.

[16] ANSI/AISC 370-21, Specification for Structural Stainless Steel Buildings, American Institute of Steel Construction (AISC), 2021.

[17] O. Zhao, S. Afshan, L. Gardner, Structural response and continuous strength method design of slender stainless steel cross-sections, Eng. Struct. 140 (2017) 14–25.

[18] ISO 13919-1:2019, Electron and laser-beam welded joints — Requirements and recommendations on quality levels for imperfections — Part 1: Steel, nickel, titanium and their alloys, European Committee for Standardization (CEN), Brussels, 2019.

[19] EN ISO 6892-1: 2016, Metallic materials: Tensile Testing – Part 1: Method of Test at Room Temperature, European Committee for Standardization (CEN), Brussels, 2016.

[20] S. Afshan, B. Rossi, L. Gardner, Strength enhancements in cold-formed structural sections — Part I: Material testing, J. Constr. Steel Res. 83 (2013) 177–188.

[21] W. Ramberg, W.R. Osgood, Description of stress–strain curves by three parameters, Natl. Adv. Commit. Aeronau. (NACA), Techn. note, 902 (1943), Washington.

[22] E. Mirambell, E. Real, On the calculation of deflections in structural stainless steel beams:

an experimental and numerical investigation, J. Constr. Steel Res. 54(1) (2000) 109–133.

[23] K.J.R. Rasmussen, Full-range stress–strain curves for stainless steel alloys, J. Constr. Steel Res. 59(1) (2003) 47–61.

[24] I. Arrayago, E. Real, L. Gardner, Description of stress–strain curves for stainless steel alloys, Mater. Des. 87 (2015) 540–552.

[25] R.D. Ziemian, Guide to stability design criteria for metal structures, 6th ed., John Wiley & Sons, 2010.

[26] Y. Sun, O. Zhao, Material response and local stability of high-chromium stainless steel welded I-sections, Eng. Struct. 178 (2019) 212–226.

[27] H.X. Yuan, Y.Q. Wang, Y.J. Shi, L. Gardner, Stub column tests on stainless steel built-up sections, Thin-Walled Struct. 83 (2014) 103–114.

[28] Y. Sun, Y. Liang, O. Zhao, Testing, numerical modelling and design of S690 high strength steel welded I-section stub columns, J. Constr. Steel. Res. 159 (2019) 521–533.

[29] B. Schafer, T. Peköz, Computational modeling of cold-formed steel: characterizing geometric imperfections and residual stresses, J. Constr. Steel. Res. 47(3) (1998)193–210.

[30] EN 1993-1-5:2006, Eurocode 3: Design of Steel Structures — Part 1-5: Plated structural elements, European Committee for Standardization (CEN), Brussels, 2006.

[31] Y. Sun, Y. Liang, O. Zhao, B. Young, Experimental and numerical investigations of S690 high-strength steel welded I-sections under combined compression and bending, J. Struct. Eng. (ASCE) 147 (2021) 04021054.

[32] Y. Sun, Y. Liang, O. Zhao, B. Young, Cross-sectional behavior of austenitic stainless steel welded I-sections under major-axis combined loading, J. Struct. Eng. (ASCE) 147 (2021)

04021202.

[33] Y. Sun, A. Su, K. Jiang, Y. Liang, O. Zhao, Testing, numerical modelling and design of stainless steel welded I-sections under minor-axis combined loading, Eng. Struct. 243 (2021) 112513.

[34] Hibbitt, Karlsson & Sorensen, Inc. ABAQUS/Standard user's Manual Volumes I-III and ABAQUS CAE Manual, Version 6.14, Pawtucket (USA); 2014.

[35] Y. Sun, A. He, Y. Liang, O. Zhao, Flexural buckling behaviour of high-chromium stainless steel welded I-section columns, Thin-Walled Struct. 154 (2020) 106812.

[36] Y. Sun, Y. Liang, O. Zhao, Local–flexural interactive buckling behaviour and resistances of high-chromium stainless steel slender welded I-section columns, Eng. Struct. 220 (2020) 111022.

[37] Y. Sun, K. Jiang, Y. Liang, O. Zhao, Experimental and numerical studies of high-chromium stainless steel welded I-section beam-columns, Eng. Struct. 236 (2021) 112065.

[38] EN 1993-1-1:2005+A1:2014, Eurocode 3: Design of Steel Structures — Part 1-1: General Rules — General rules and rules for buildings, European Committee for Standardization (CEN), Brussels, 2014.

[39] ANSI/AISC 360-16, Specification for Structural Steel Buildings, American Institute of Steel Construction (AISC), 2016.

[40] S. Afshan, L. Gardner, The continuous strength method for structural stainless steel design, Thin-Walled Struct. 68 (2013) 42–49.

[41] B.W. Schafer, S. Ádány, Buckling analysis of cold-formed steel members using CUFSM:

conventional and constrained finite strip method, 18th Int. Spec. Conf. Cold-Formed Steel Struct. (2006).

[42] M.R. Bambach, K.J. Rasmussen, V. Ungureanu, Inelastic behaviour and design of slender I-sections in minor axis bending, J. Constr. Steel Res. 63 (1) (2007) 1–12.

[43] M. Gkantou, M. Bock, M. Theofanous. Design of stainless steel cross-sections with outstand elements under stress gradients, J. Constr. Steel Res. 179 (2021) 106491.

[44] EN 1990:2002+A1:2005, Eurocode – Basis of structural design, European Committee for Standardization (CEN), Brussels, 2005.

[45] S. Afshan, P. Francis, N.R. Baddoo, L. Gardner, Reliability analysis of structural stainless steel design provisions, J. Constr. Steel Res. 114 (2015) 293–304.

Figures

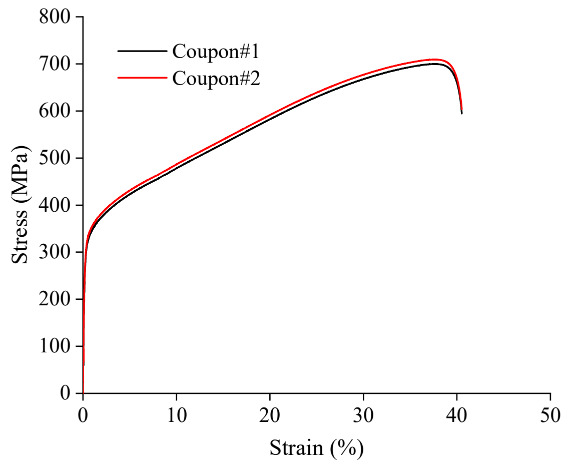

Fig. 1. Measured stress–strain curves.

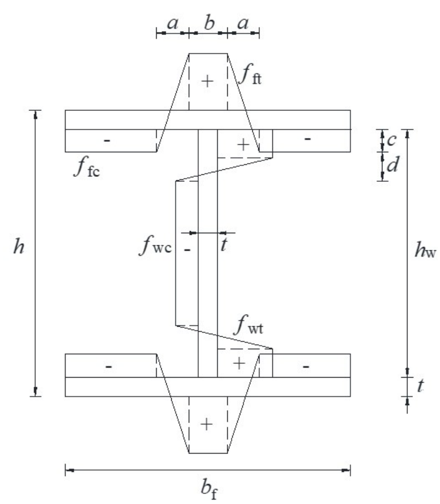

Fig. 2. Membrane residual stress predictive model for laser-welded stainless steel I-sections (+ve = tension; -ve =compression).

Fig. 3. Setup for initial local geometric imperfection measurements.

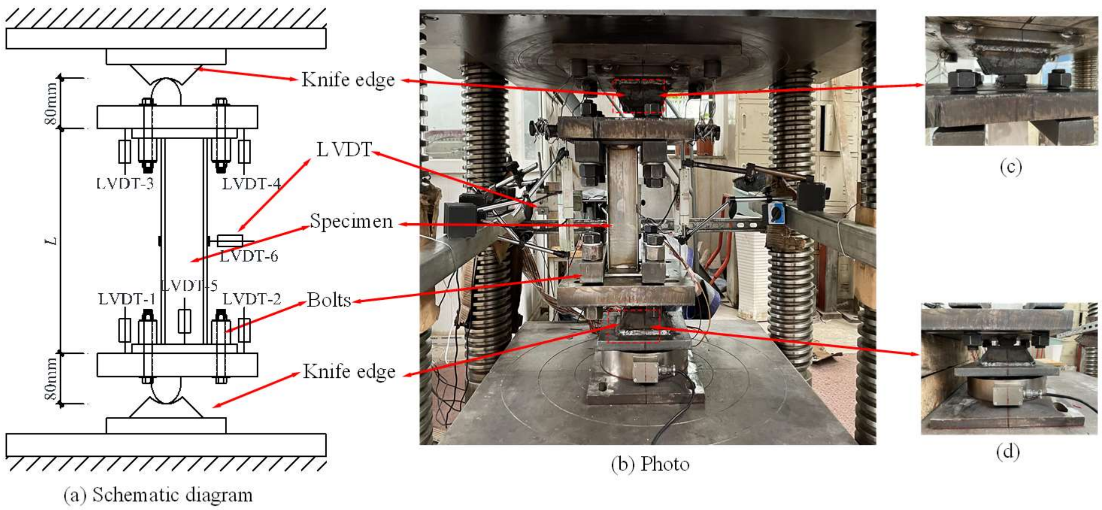

Fig. 4. Eccentric compression test setup.

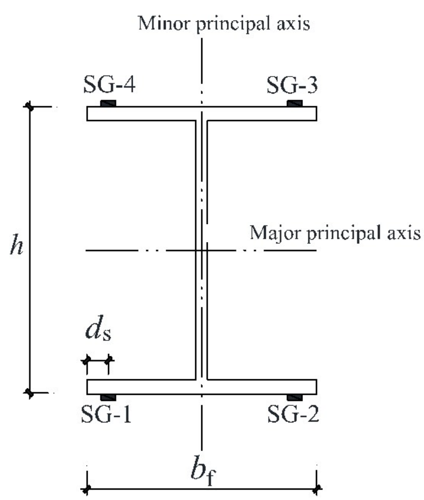

Fig. 5. Detailed positions of strain gauges.

(a) Minor-axis combined loading

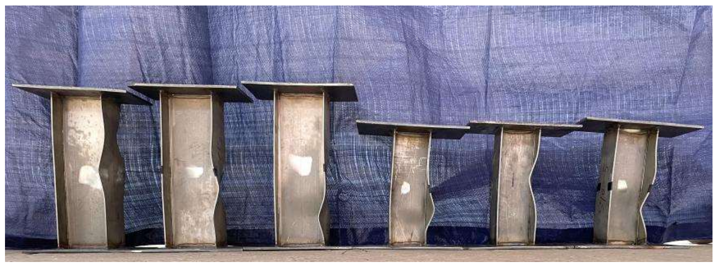

(b) Major-axis combined loading

Fig. 6. Failure modes of laser-welded stainless steel slender I-section stub column specimens under combined loading.

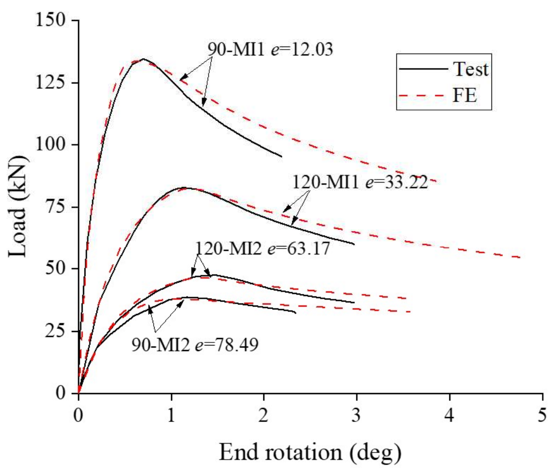

(a) Minor-axis combined loading

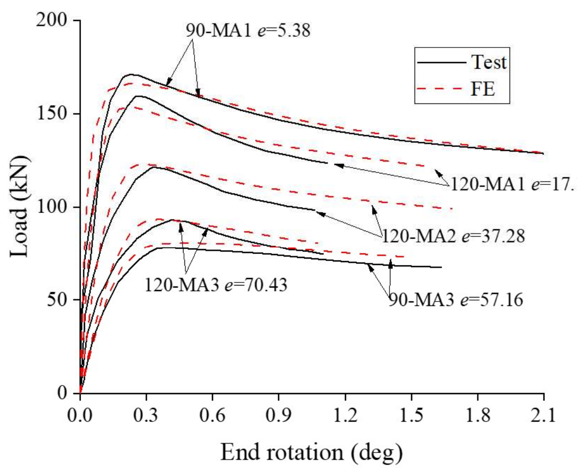

(b) Major-axis combined loading

Fig. 7. Load–end rotation curves of laser-welded stainless steel slender I-section stub column specimens under combined loading.

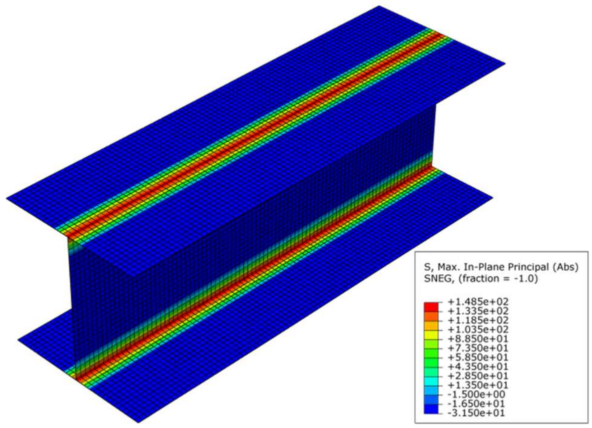

Fig. 8. Typical membrane residual stresses (in MPa) for modelled I-90×90×3 specimens.

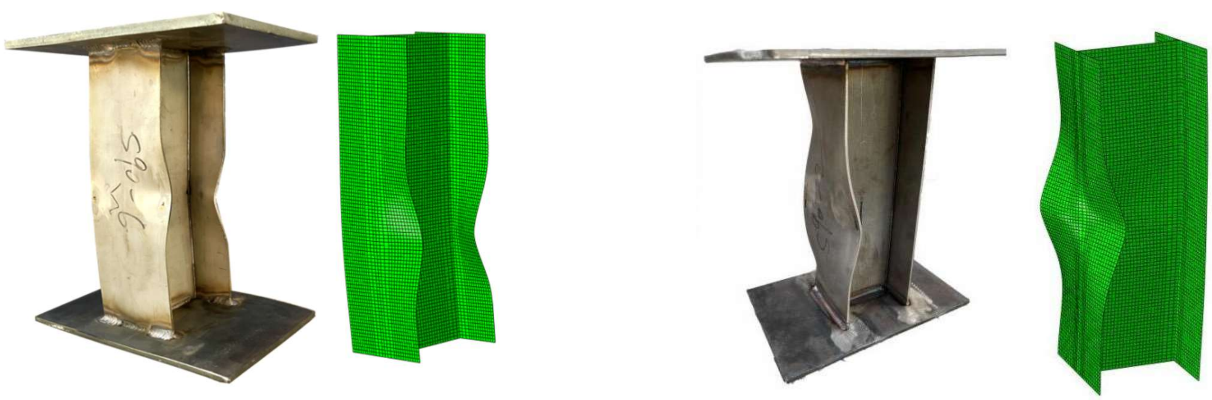

(a) Specimen 90-MI2 (minor-axis combined loading) (b) Specimen 90-MA3 (major-axis combined loading)

Fig. 9. Test and FE failure modes of typical specimens under combined loading.

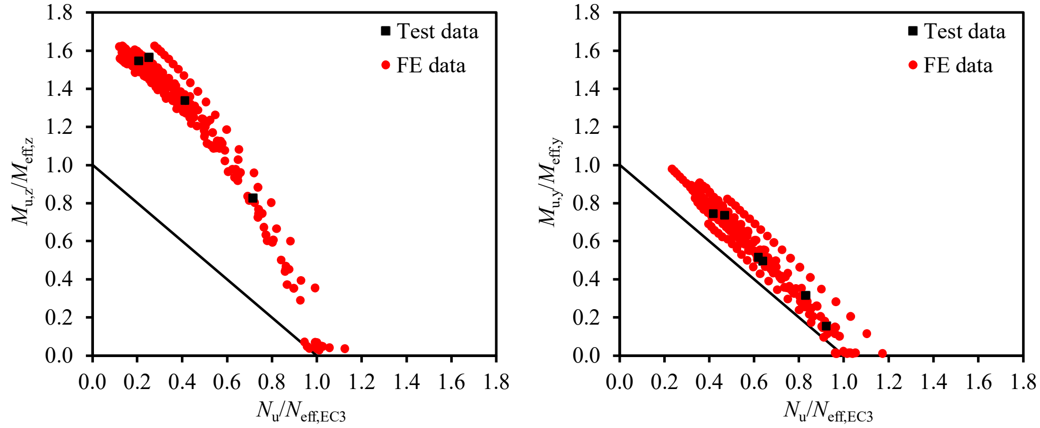

(a) Minor-axis combined loading

(b) Major-axis combined loading

Fig. 10. Comparisons of test and numerical failure loads with EC3 predicted failure loads.

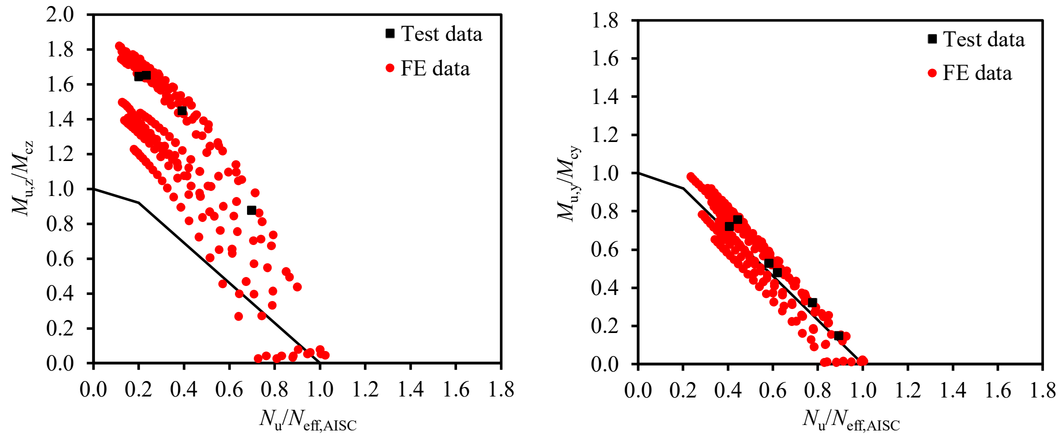

(a) Minor-axis combined loading

(b) Major-axis combined loading

Fig. 11. Comparisons of test and numerical failure loads with AISC predicted failure loads.

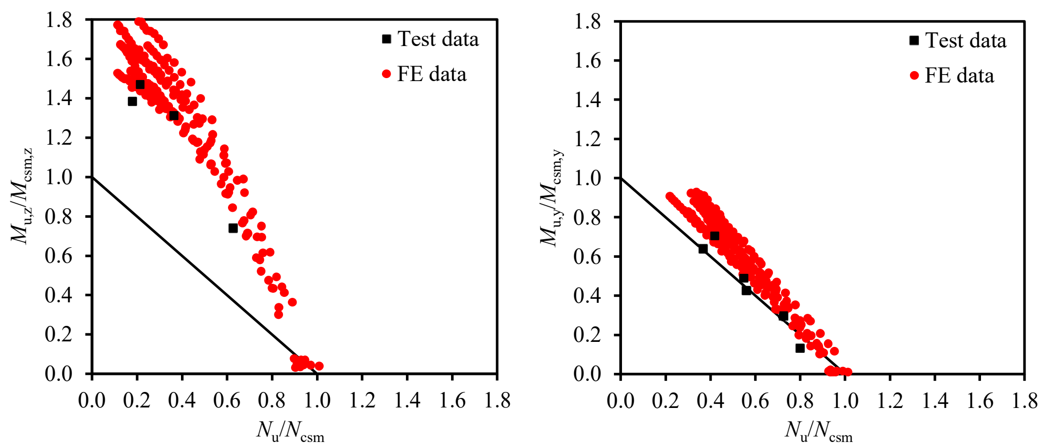

(a) Minor-axis combined loading

(b) Major-axis combined loading

Fig. 12. Comparisons of test and numerical failure loads with CSM predicted failure loads.

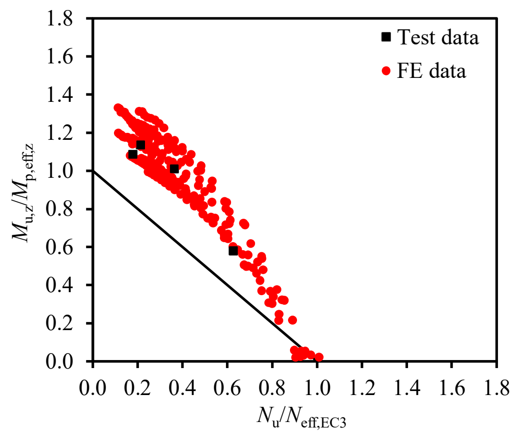

Fig. 13. Comparisons of test and numerical failure loads with new proposal predicted failure loads.

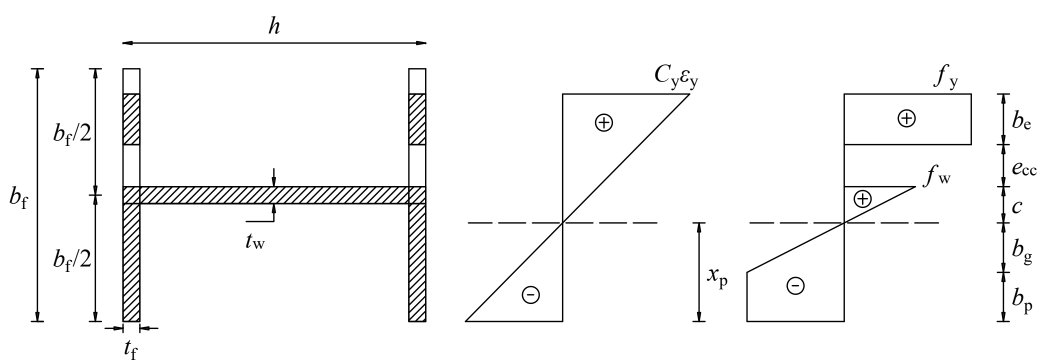

Fig. 14. Strain and stress distributions in slender flanges.

Tables

Table 1

Key average measured material properties.

E (MPa)	f_y (MPa)	$f_{1.0}$ (MPa)	f_u (MPa)	ε_u (%)	ε_f (%)	R–O coefficients n	$m_{1.0}$
189000	297	349	704	38	60	5.3	2.9

Table 2

Membrane residual stress predictive model for laser-welded stainless steel I-sections [6].

$f_{ft} = f_{wt}$ (tension)	$f_{fc} = f_{wc}$ (compression)	a	b	c	d
$0.5f_y$	From equilibrium	$0.1b_f$	$0.075b_f$	$0.0375h_w$	$0.1h_w$

Table 3

Geometric properties of laser-welded stainless steel slender I-section stub column specimens under combined loading.

Axis of combined loading	Cross-section	Specimen ID	L (mm)	h (mm)	b_f (mm)	t (mm)	ω_0 (mm)	ω_0/b_f
Minor axis	I-90×90×3	90-MI1	270.1	89.22	90.00	2.76	0.30	1/300
	I-90×90×3	90-MI2	269.2	89.18	89.97	2.75	0.23	1/391
	I-120×90×3	120-MI1	360.1	119.40	89.97	2.81	0.25	1/360
	I-120×90×3	120-MI2	361.2	119.48	90.08	2.72	0.28	1/322
Major axis	I-90×90×3	90-MA1	270.5	89.39	90.05	2.74	0.35	1/257
	I-90×90×3	90-MA2	270.0	89.51	90.01	2.75	0.26	1/346
	I-90×90×3	90-MA3	270.0	89.27	89.95	2.75	0.26	1/345
	I-120×90×3	120-MA1	359.8	119.51	89.94	2.76	0.31	1/290
	I-120×90×3	120-MA2	360.0	119.27	89.93	2.79	0.30	1/300
	I-120×90×3	120-MA3	360.0	119.20	89.91	2.81	0.28	1/321

Table 4

Key test results for laser-welded stainless steel slender I-section specimens under combined loading.

Axis of combined loading	Specimen ID	e_0 (mm)	N_u (kN)	Δ_u (mm)	M_u (kNm)	δ_u (mm)	ϕ_u (deg)
Minor axis	90-MI1	12.03	134.53	3.23	2.05	0.85	0.69
	90-MI2	78.49	38.61	4.46	3.20	3.36	1.09
	120-MI1	33.22	82.76	3.87	3.07	1.68	1.15
	120-MI2	63.16	47.47	4.12	3.19	3.22	1.49
Major axis	90-MA1	5.38	170.93	0.31	0.97	1.03	0.23
	90-MA2	25.04	119.47	1.58	3.18	– *	– *
	90-MA3	57.16	78.13	2.58	4.67	1.89	0.46
	120-MA1	17.17	159.49	1.11	2.92	0.97	0.29
	120-MA2	37.28	121.42	2.21	4.79	1.41	0.40
	120-MA3	70.43	93.09	3.32	6.86	1.83	0.46

* LVDTs were disconnected to data logger during testing – LVDT readings could not be obtained.

Table 5

Comparison between test and numerical failure loads for measured and generalised local imperfection magnitudes.

Axis of combined loading	Specimen ID	FE N_u / Test N_u	
		ω_0	$b_f/300$
Minor axis	90-MI1	1.00	1.01
	90-MI2	1.02	1.02
	120-MI1	1.00	1.00
	120-MI2	1.02	1.01
Major axis	90-MA1	1.02	1.03
	90-MA2	0.98	0.98
	90-MA3	1.00	1.00
	120-MA1	1.04	1.04
	120-MA2	0.99	0.99
	120-MA3	0.96	0.96
	Mean	1.01	1.01
	COV	0.02	0.02

Table 6

Cross-section dimensions and loading eccentricities of modelled laser-welded stainless steel slender I-sections in parametric studies.

h (mm)	b (mm)	t (mm)	e_0 (mm)
60, 90, 120, 150	60, 90, 120, 150	2, 2.2, 2.4, 2.6, 2.8, 3	1, 5, 10, 15, 20, 25, 30, 35, 40, 45, 50, 55, 60, 65, 70, 75, 80, 85, 90, 95, 100

Table 7

Comparisons of test and numerical failure loads with predicted failure loads.

(a) EN 1993-1-4 [15]				
Loading condition	No. of test data	No. of FE data	$N_u/N_{u,pred}$	
			Mean	COV
Minor-axis combined loading	4	200	1.64	0.11
Major-axis combined loading	6	200	1.15	0.09

(b) AISI/AISC 370-21 [16]				
Loading condition	No. of test data	No. of FE data	$N_u/N_{u,pred}$	
			Mean	COV
Minor-axis combined loading	4	200	1.61	0.16
Major-axis combined loading	6	200	1.11	0.08

(c) CSM [17]				
Loading condition	No. of test data	No. of FE data	$N_u/N_{u,pred}$	
			Mean	COV
Minor-axis combined loading	4	200	1.58	0.11
Major-axis combined loading	6	200	1.12	0.07

(d) New proposal				
Loading condition	No. of test data	No. of FE data	$N_u/N_{u,pred}$	
			Mean	COV
Minor-axis combined loading	4	200	1.21	0.07

Table 8

Reliability analysis results for new design method according to EN 1990 [44].

No. of test and FE data	$k_{d,n}$	b	V_δ	V_r	γ_{M1}
204	3.14	1.17	0.11	0.13	0.99